Experimental Mechanics (2019) 59:775–790
https://doi.org/10.1007/s11340-019-00495-2

Novel Capability for Microscale *In-situ* Imaging of Temperature and Deformation Fields under Dynamic Loading

A. Keyhani[1] · R. Yang[1] · M. Zhou[1]

Received: 9 November 2018 / Accepted: 10 February 2019 / Published online: 12 March 2019

Abstract

To understand the mesoscale mechanisms responsible for the behavior of heterogeneous materials and to validate models, it is important to experimentally measure the deformation and temperature fields at the microstructure level. So far, there has been no methods that can yield such measurements simultaneously for dynamic experiments. Here, we report the development of a novel capability for simultaneous time- and space-resolved recording of both fields over the same microstructure area of a sample with micron-level spatial resolutions and microsecond time resolutions. Referred to as MINTED (**M**icroscale ***In-situ*** Imaging of Dynamic **Te**mperature and **D**eformation Fields), the system cohesively integrates a high-speed visible light (VL) camera and a state-of-the-art high-speed infrared (IR) camera via a custom-designed dichroic beam splitter-lens assembly. The combined VL and IR images allow the deformation fields to be obtained through digital image correlation (DIC) and the temperature fields over the same area to be obtained through pixel-level calibration of the differing emissivities of heterogeneous constituents in microstructures. Experiments are conducted on granular sucrose in a Kolsky bar [or split-Hopkinson pressure bar (SHPB)] environment, yielding both microstructure level fields along with overall material response. The strain and temperature fields provide detailed first-time insight into the processes of fracture, friction, shear localization, and hotspot development in the microstructures.

Keywords Dynamic thermo-mechanical response · High-speed visible and infrared imaging · Split-Hopkinson pressure bar (SHPB) · Heterogeneous materials (HM) · Sucrose

Introduction

The thermo-mechanical response of heterogeneous materials under dynamic loading is of great importance in many applications. Dynamic loading events can cause severe damage and energy dissipation, leading to the formation of temperature spikes in a wide range of materials, including, e.g., metals [1–4], polymers [5], composites [6], ceramics [7], shape memory alloys (SMAs) [8, 9], and energetic materials [10, 11]. One class of temperature spikes are referred to as hotspots, and can cause thermal softening, thermal runaway, or even the onset of chemical reactions in energetic materials [12]. Local failure and formation of temperature spikes result from several factors, such as strain localization due to heterogeneity in the microstructure, material property mismatch between constituents, and the existence of defects such as voids, cracks and inclusions. Field et al. [10, 11] provided evidence for the mechanisms contributing to the formation of hotspots. Subsequently, computational and experimental approaches have been widely used to study mechanisms responsible for heat generation in heterogeneous materials. Specifically for energetic materials, computational studies have enhanced understanding of heating mechanisms. However, these studies are limited in terms of the resolution of fine-scale physics and require experimental data for calibration and validation. On the other hand, experiments have provided insights into underlying heating mechanisms. For example, it is known that inelasticity [13, 14], void collapse, inter-particle contact, and internal fracture and friction [15, 16] are dominant heating mechanisms in energetic materials and other heterogeneous materials. However, experiments have not allowed full understanding and detailed quantification of the underlying mechanisms primarily due to the lack of abilities to directly measure, in time- and space-resolved manner, the thermal and mechanical fields at the microstructural level for dynamic conditions.

✉ M. Zhou
min.zhou@gatech.edu

[1] The George W. Woodruff School of Mechanical Engineering, School of Materials Science and Engineering, Georgia Institute of Technology, Atlanta, GA 30332-0405, USA

The experimental study of the thermo-mechanical response of such heterogeneous materials at the microstructure level under dynamic loading has been especially challenging due to limitations of existing techniques for deformation and temperature measurements at high speeds and high spatial resolutions over the same area of a sample. As a result, dynamic experiments have been limited to either mechanical deformation or thermal responses. Specifically, these experiments have been based on indirect/implied correlations between deformation mechanisms and thermal responses [11, 15, 17], without quantitative measurements that can directly relate the mechanical and thermal events.

For time-resolved temperature measurements in dynamic experiments, researchers have used several approaches including embedded electrical sensors [18, 19], optical pyrometry [20], Raman spectroscopy [21], Neutron resonance spectroscopy [22], and reflectance thermometry [23, 24]. All of these approaches have some advantages and disadvantages. For example, embedded electrical sensors can measure the temperature of a sample with high accuracy and is independent of the sample properties. However, thick sensors do not equilibrate with the sample quickly enough and thin sensors may break before or during experiments, as a result, the technique cannot be used for highly dynamic events. This challenge can be avoided by using non-contact approaches including optical pyrometry and Raman spectroscopy. However, these non-contact approaches so far offer bulk average measures, require the knowledge of the sample properties such as radiance and emissivity, and do not offer high spatial resolutions. The reflectance thermometry approach uses light reflected from the sample rather than radiation emitted by the sample, which does not require knowledge of the properties of the sample but again requires the adherence of an extrinsic material on the sample and depends on thermal equilibration between the sample and the extrinsic material film [23, 24]. None of these methods allow simultaneous recording of both deformation and temperature fields over an area of a sample's microstructure.

The work by Coffey and Jacobs [25] was an early attempt to estimate the temperature achieved during deformation in impact experiments. The technique uses heat-sensitive films which darken upon exposure to heat. Since darkening levels of the heat-sensitive films depend on both temperature and time, the time of deformation must be known to estimate temperature levels based on calibration curves. Later, heat-sensitive films along with high-speed photography were used to study primary failure mechanisms in polymer bounded explosives (PBXs) at the macroscale [10]. However, this technique cannot reveal the underlying mechanisms at micron levels. In the 1980s and 1990s, advances in infrared detectors made it possible to measure temperature in real time with microscale spatial resolutions. For example, Marchand and Duffy [2], Zehnder and Rosakis [26] and Zhou et al. [3] used an integrated system of infrared thermal detectors to measure temperature variations along lines across cracks and shear bands in metals. High-speed photography was also used to study the associated mechanical processes, but at different (larger) size scales.

Measuring temperatures of a material with thermocouples, spot pyrometers, heat sensitive films, or infrared temperature detectors along lines or over small areas has provided useful information and insight. The measurements, to various degrees, are averaged over space and time, or only available over small domains. For example, Costin et al. [27] used only one infrared detector and homogenized the temperature over a spot size of 1 mm. Later, Hartley et al. [1] used a linear array of infrared detectors and measured the temperature over a spot size of 20 μm. Similarly, Merchand and Duffy [2], and Zhou et al. [3] used linear arrays of 12-16 infrared detectors with spot sizes of $35-100$ μm. In the first spatial temperature measurement effort, Guduru et al. [4] developed and used a spatial array of 8×8 infrared detectors, with each detector measuring the average temperature over an area of 110×110 μm. These methods are quite advanced and are still in further development. However, so far the spatial or temporal resolutions certainly show need for significant improvement before full characterization of events at the microstructure level at high loading rates are possible. In particular, for heterogeneous materials, the differing emissivities of multiple constituents must be accounted for in order for correct temperatures to be obtained. This task requires an independent image of the evolving material microstructure that is in addition to the IR image as deformation occurs. Existing capabilities do not offer such independent images.

For quasi-static conditions, infrared (IR) cameras have been used along with visible light (VL) cameras for simultaneous temperature and deformation measurements. For example, an experimental environment consist of VL and IR cameras was used to measure temperature and deformation fields during glass forming [28]. The VL and IR imaging was not at normal incidence since the cameras have different angles of view. Further, the measurement was macroscopic and not microscopic. A dichroic mirror was used to separate VL and IR emissions from the sample surface to achieve imaging at normal angle [29, 30] in a setup for quasi-static conditions with a maximum stain rate of 5×10^{-3} s^{-1}. High-speed infrared cameras have recently developed to a point where capturing time- and space-resolved measurements over areas on the order of millimeters is now possible, at resolutions of microns and microseconds. Although the IR imaging capabilities are still not on par with visible spectrum imaging, simultaneous measurements for deformations rates on the order of 10^3 s^{-1} typical of Kolsky bar (or split-Hopkinson bars) can be achieved.

The split-Hopkinson pressure bar (SHPB) or Kolsky bar apparatus (KBA) is a well-established experimental technique for characterizing materials and structures under dynamic

loads. The SHPB apparatus was established by Hopkinson [31], with further developments by Kolsky [32]. Since its advent, it has been improved and extended for a wide range of applications such as dynamic compression and tension tests [33, 34], torsion tests (torsional split-Hopkinson bar or TSHB) [35, 36], the Brazilian test [37, 38], fracture toughness measurements [39–41], wave separation and dispersion tests [42–44], dynamic loading experiments on geotechnical materials [45] and soft materials [46], and other high strain rate experiments [47]. The SHPB apparatus or the KBA provides stress-strain, strain-time, and strain rate-time relations [48], which can be used to validate constitutive relations of materials at high strain rates [49]. The SHPB apparatus also has been used along with infrared detectors to analyze the overall thermo-mechanical response of materials [5, 6]. The classic devices allow for only macro-scale analyses of dynamic response of materials. For meso-scale analyses of deformation in materials, the SHPB apparatus has been used along with high-speed photography [17, 38, 49, 50] and high-speed x-ray imaging [51].

In this paper, we report the development of a novel capability for simultaneous, time-resolved and space-resolved recording of both the temperature field and the deformation field over the same microstructure area of a sample with micron-level spatial resolutions and microsecond temporal resolutions. Referred to as MINTED (**M**icroscale ***In-situ*** Imaging of Dynamic **Te**mperature and **D**eformation Fields), the system cohesively integrates a high-speed visible light (VL) camera and a state-of-the-art high-speed infrared (IR) camera via a custom-designed dichroic beam splitter-lens assembly. The combined VL and IR images allow the deformation fields to be obtained through digital image correlation (DIC) and the temperature fields over the same area to be obtained through pixel-level calibration of the differing emissivities of heterogeneous constituents in microstructures. Experiments are conducted on granular sucrose which is widely used as a simulant of energetic crystals [52] in a KBA or SHPB environment, yielding both microstructure level fields along with overall material response. The strain and temperature provide detailed first-time insight into the processes of fracture, friction, shear localization, and hotspot development in the microstructures. In particular, the correlation between hotspots, microstructure, and local deformation mechanisms is analyzed.

Experimental Layout

The overall configuration of the MINTED system in a SHPB environment is illustrated in Fig. 1. To simultaneously capture deformation and temperature fields, the visible (VL) and infrared (IR) parts of the emission spectrum from the sample pass through a sapphire window and are separated by a dichroic beam splitter. VL is reflected and IR is transmitted. The VL reflection efficiency of the dichroic beam splitter and the IR transmission efficiency are both greater than 85%. The VL camera is mounted vertically, while the IR camera is mounted horizontally, directly facing the sample surface. The sample is encased in a specimen holder, as discussed later. The IR emission passes through a set of custom-designed correction lenses to correct wave-front distortions induced by the non-normal incidence of the IR beam at the beam splitter which has a finite thickness. The IR and VL cameras are synchronized in time and calibrated in spatial positions (see below), consequently, the VL and IR images can be coordinated for the extraction of the deformation and temperature fields. A triggering system is designed and built to operate the two cameras simultaneously. Two sets of sensors are placed close to the incident bar to detect the motion of the bar and trigger the cameras and other devices via a control box. The control box also activates electric solenoid valves to run an air gun to start the experiment and secure the loading mechanism. Illustrations and pictures of the experimental setup are shown in Figs. 1 and 2, respectively.

High-Speed Photography of Deformation Fields

A Phantom v2512 camera, which can operate at 25,700 fps at 1 megapixel (MP) resolution and 1,000,000 frames per second (fps) at 128 × 32 pixels, is used to record the VL images. An Infinity K1 long-distance microscope lens is used along with the VL camera to zoom in far enough to capture high-resolution micro-scale images. The VL lens magnification factor is 2.09 and the working distance is 145 mm. The VL images are captured by the high-speed camera, with a frame rate of 100,000 fps, a spatial resolution of 13.4 μm, and a field of view (FOV) of 6.9 × 4.3 mm to record the deformation of the sample.

Selecting a proper illumination light source for high-speed imaging in this experimental layout is challenging. A sufficiently bright light source is necessary at framing rates around 100,000 fps; however, due to the high level of heat generation by a powerful light source, temperature measurements are likely to be affected. In addition, the custom-designed dichroic beam splitter-lens assembly is very close to the specimen confinement box and the sample (< 5 mm), leaving only a very tight space for an illuminating light source. To overcome these challenges, four LED light sources along with fiber optics are used. The LED light sources are placed far from the sample, and the light is projected onto the sample through optical fibers, as shown in Fig. 2. This configuration minimizes heating relative to other light sources, such as halogen lights, and permits proper placement within the tight space of the experimental setup. We tested the temperature interference of three available lighting options including fiber-optic halogens, LED panels, and fiber-optic LEDs, the latter of which has the least effect on the sample temperature (see Fig. 3).

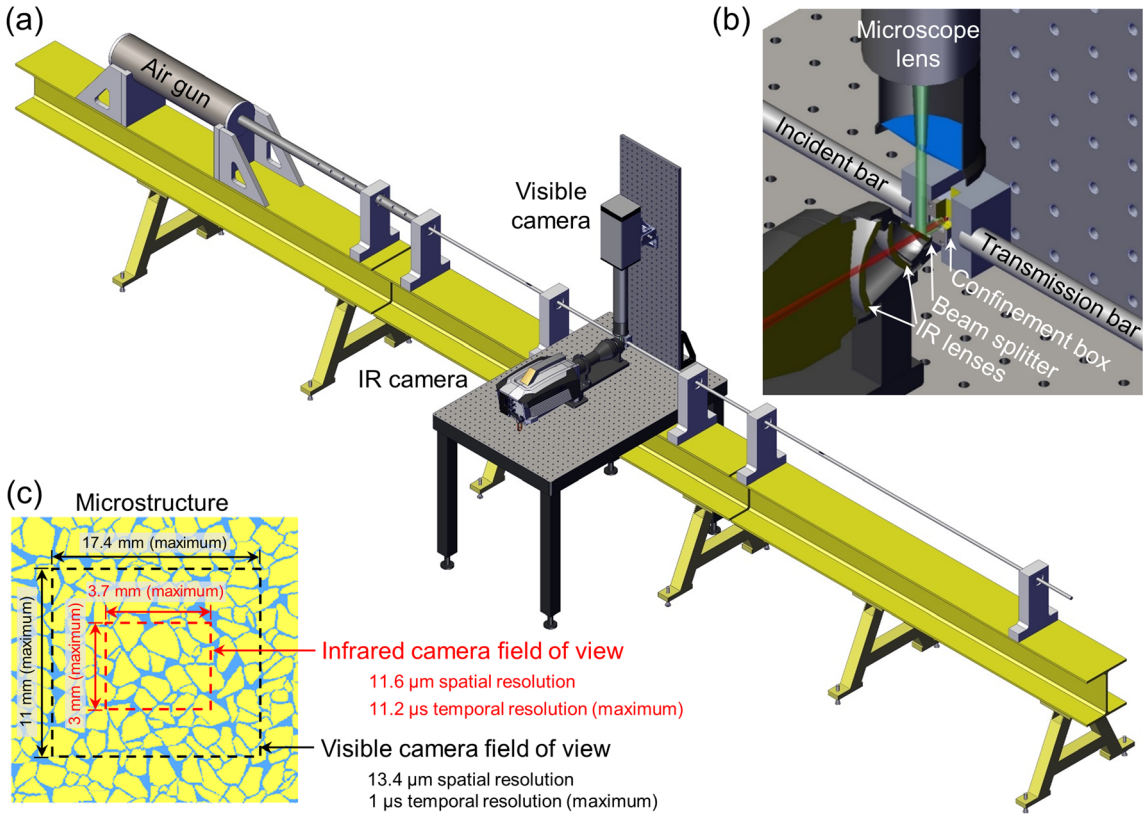

Fig. 1 Experimental setup for simultaneous high-speed infrared (IR) and visible (VL) imaging of microscale temperature and deformation fields under dynamic conditions; (**a**) configuration of the split-Hopkinson bar apparatus and visible and infrared cameras, (**b**) relative positons of the confinement box, the dichroic beam splitter, the visible microscope lens, and the infrared lens assembly, and (**c**) relative positions of visible and infrared fields of view

Since the system of integrated VL and IR cameras can also be used for quasi-static experiments, the temperature interference analysis of the illumination is carried out over a relatively long period of 10 min (Fig. 3). The fiber-optic LEDs used result in a 0.2 K increase in the temperature of the sample after 10 min. However, for the experiments conducted, the illuminating

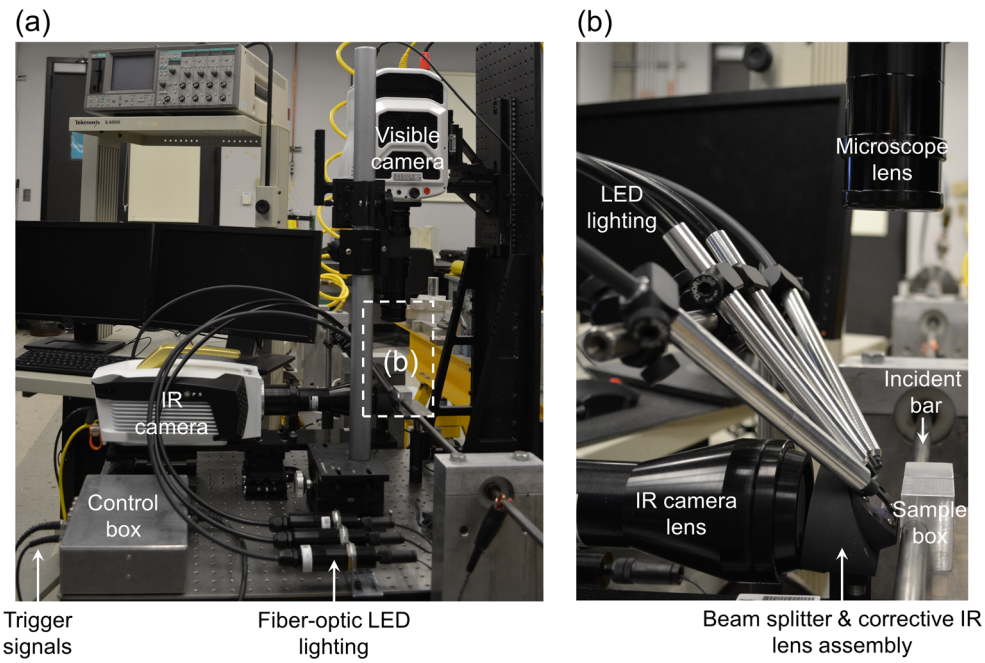

Fig. 2 Pictures of the MINTED experimental system; (**a**) overall view of the components, and (**b**) close-up view of the dichroic beam splitter, the VL and IR lenses, and LED lighting

lights are activated for only a few milliseconds; therefore, the resulting effect on temperature measurements is essentially undetectable.

High-Speed Temperature Measurements

A Telops M2k high-speed thermal imaging camera (Telops Inc., Quebec, Canada) is used to record the IR images. This camera operates at 2000 fps with a spatial resolution of 320 × 256 pixels and 90,000 fps with a spatial resolution of 64 × 4 pixels. An IR microscope lens with the magnification factor of 2 and the working distance of 50 mm is used. The IR camera is calibrated along with the IR microscope lens, the corrective IR lenses, the dichroic beam splitter, and the sapphire window. The IR camera operates at 5000 fps with an 11.6 μm spatial resolution and an 1.5 × 1.5 mm FOV. At these settings, the accuracy of the temperature measurements is 0.5 K according to calibration data. Since the IR camera is calibrated to blackbody emission, the camera reading must be reinterpreted using the emissivity of the sample's constituents in order to arrive at the correct temperature field for real samples. The emissivity of the sample material (sucrose) is determined to be ~0.97 by calibrating the camera reading to the initial (known) temperature of the sample. The calibration is based on the Stefan-Boltzmann law in the form of

$$E = e\sigma T_s^4, \tag{1}$$

where E is the power flux recorded by the IR camera, e is the emissivity of the particular material constituent at a particular pixel of an image, σ is the Stefan-Boltzmann constant, and T_s is the temperature of the sample at the pixel of interest. The relation between the camera's temperature reading T_c for the pixel and the actual sample temperature T_s at the pixel is $\sigma T_c^4 = e\sigma T_s^4$ yielding

$$T_s = \frac{T_c}{\sqrt[4]{e}}. \tag{2}$$

This analysis assumes the emissivity remains constant during the deformation. It is believed that changes in the emissivity at low temperatures are negligible. More accurate determination of the emissivity and emissivity changes is the subject of our future studies.

Visible and Infrared Images Synchronization in Space and Time

Figure 4 illustrates the electrical system of the experimental setup. The control box sends triggering signals to the VL and IR cameras, the oscilloscope, and the gas gun solenoids. The same reference time is required for both cameras to allow for synchronization of the VL and IR images in time. For spatial correlations of the VL and IR images, we use two calibration targets that can be identified by both cameras. The targets are visible in the VL and IR images due to differing colors and emissivity differences between different colors. Figure 5(a) and (b) show the VL and IR images of a target used to measure the spatial resolutions (pixel sizes) of both cameras, respectively. To set a reference coordinate for both images, we used a star sector target and moved the center pixels of the FOVs of both cameras to the center of the target [Fig. 5(c) and (d)]. Using this reference coordinate and the pixel size of both the VL and IR images, we spatially synchronized the captured VL and IR images (Fig. 6) for actual material samples. In general, the IR images are not as sharp as the VL images.

Materials

Experiments were conducted on sucrose ($C_{12}H_{22}O_{11}$) granules with a molecular weight of 342.3 g/mol. Sucrose is a commonly used simulant for HMX energetic crystals in impact experiments [52]. The material is purchased from Research Products International (RPI). The granules are graded using standard AASHTO sieves and three sets of samples with the average grain sizes of 165, 362.5, and 775 μm are selected for the experiments. Figure 7 shows the initial density and average grain size of the three sets. The deformation of the sucrose granules is crystallographically dependent. The elastic modulus of sucrose single crystals on the (100) crystallographic plane is 38 GPa and the modulus on the (001) plane is 33 GPa [53]. The onset of shear stress causing plastic deformation in sucrose grains is 1 GPa [53].

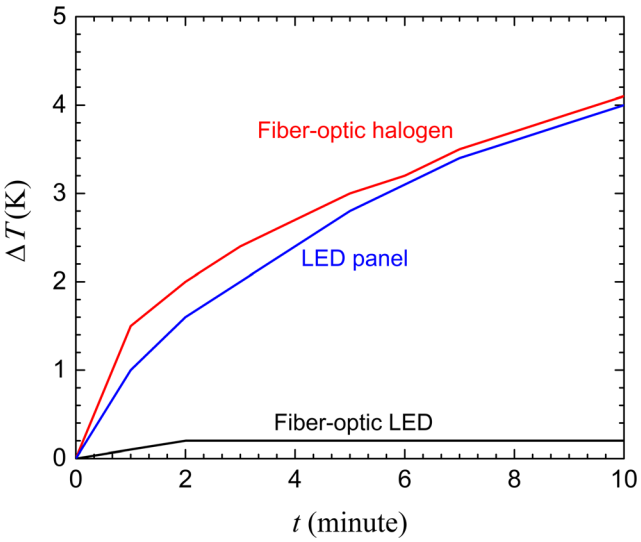

Fig. 3 Comparison of the temperature increases in a sample as a result of different lighting schemes, LED is chosen due to its negligible effect

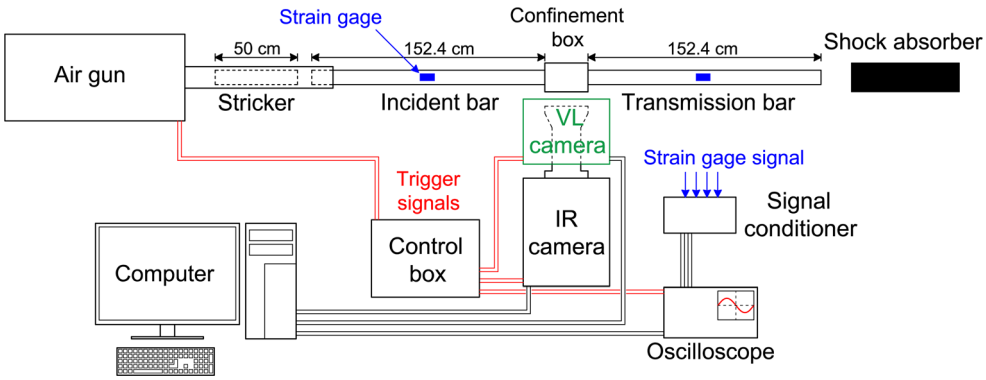

Fig. 4 Schematic illustration of electrical and control devices

Loading Configuration

A classic compression split-Hopkinson bar (SHPB) or Kolsky bar setup is used for the dynamic compression of the samples as discussed below. The striker (projectile), and incident and transmission bars are made from the C350 maraging steel with a density of $\rho = 7800$ Kg/m^3 and a Young's modulus of $E = 210$ GPa, yielding a bar wave speed of $c = \sqrt{E/\rho} = 5188$ m/s. The length of the striker is $L_{st} = 50$ cm. With this configuration, the duration of the generated compressive pulse in the incident bar is $\tau = 2L_{st}/c = 0.2$ ms. The length and the diameter of each bar (incident and transmission) is 152.4 cm (5 ft) and 1.27 cm (0.5 in), respectively.

The Sucrose grains are confined in a box with a sapphire window. Loading is through two indenters, as illustrated in Fig. 8. The internal dimensions of the confinement box are $5 \times 7 \times 5$ mm. The confinement box is designed such that the ends of the incident bar and the transmission bar are placed inside the indenters (not visible). This design prevents lateral movements of the confinement box and the sample relative to the lenses in order to ensure the safety of the optics and in order to maintain the focal distance between the sample and the lenses necessary for capturing sharp images. The relative positions of the confinement box, the incident bar, and the transmission bar are shown in Fig. 1(b). The maximum overall strain rate in the experiments carried out is 1260 ± 90 s^{-1}.

In a standard SHPB apparatus, the overall stress, strain and strain rates in the sample can be calculated using the signals obtained by strain gages mounted on the bars. A requirement for this calculation is that the sample is relatively small and

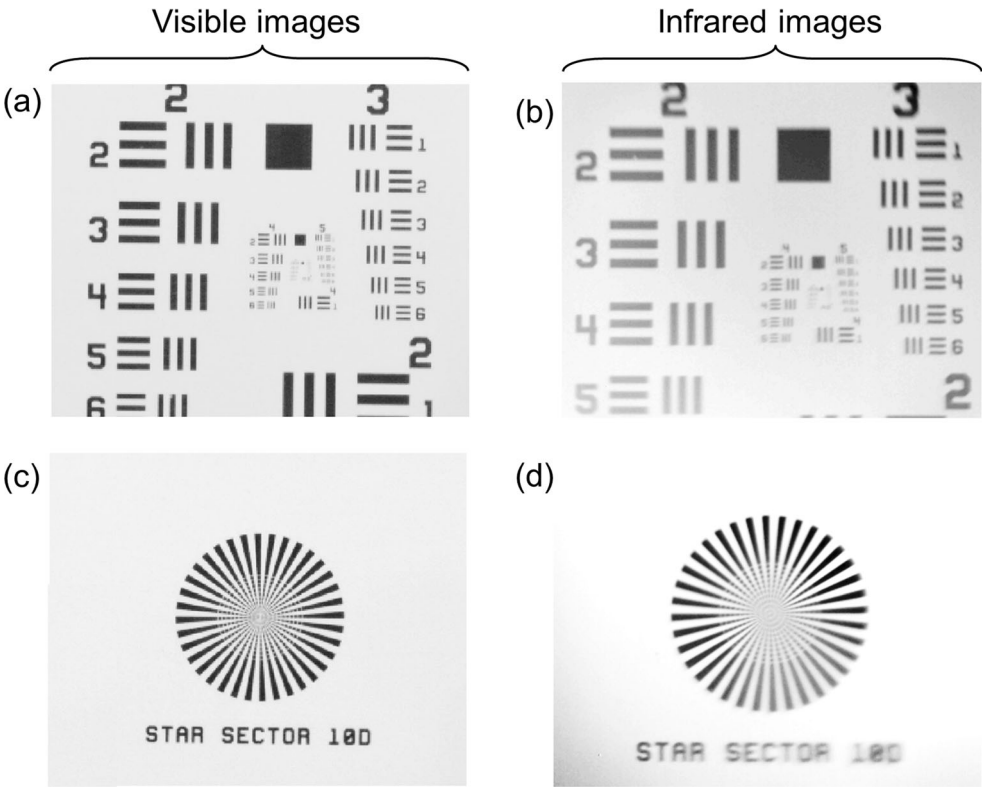

Fig. 5 (**a**) and (**b**): visible and infrared images of a target for resolution determination, respectively. (**c**) and (**d**): visible and infrared images of a star sector target for alignment, respectively. The resolution of all images is 320×256 pixels

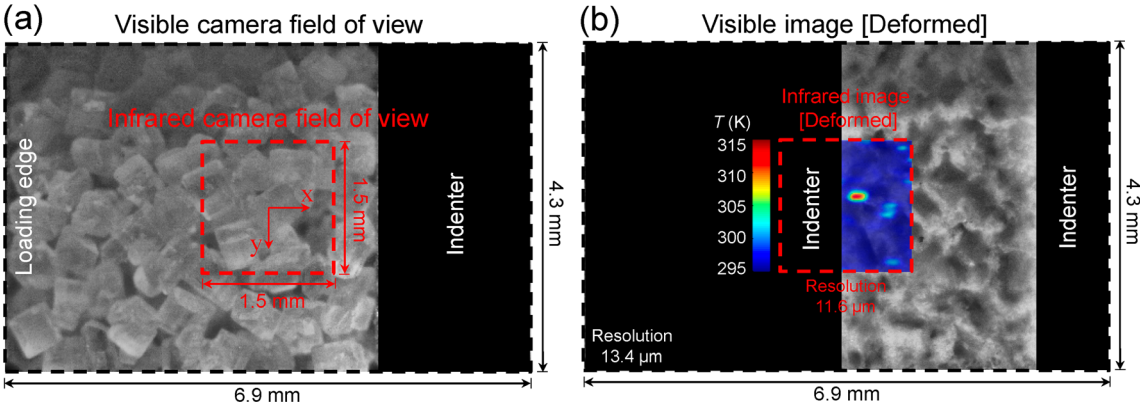

Fig. 6 Relative positions of visible and infrared fields of view for (**a**) the undeformed sample and (**b**) the deformed sample

wave reverberations due to impedance mismatch between the bars and the sample are equilibrated quickly. In this work, the confinement box causes the wave reverberations to be more significant relative to cases without the confinement box. As such the standard calculations are less accurate. In this paper, the overall strain and strain rate in the samples are calculated based on the relative distance of the indenters (engineering strain, $\Delta L/L_0$, where $L_0 = 5$ mm is the initial length of the sample in the loading direction). The relative distance between the indenters are obtained from the VL images. This is more accurate than using the bar signals. As for stress, we chose to be silent rather than reporting less than reliable readings and focus on the deformation and heating at the microstructure level instead. It is certainly desirable to obtain the overall stress on the sample in the future.

Results and Discussion

The experiments here focus on the evaluation of the capabilities of the developed MINTED system. We begin by subjecting the three materials to loading under the conditions discussed above. The recorded images are computationally analyzed. The temperature fields reported here reflect interpretation accounting for the emissivity effect based on equation 2. The temperature fields are analyzed in conjunction with the deformation fields to correlate the locations of hotspots with microstructure features. Digital image correlation (DIC) analyses are carried out to obtain the strain fields for comparison with the temperature fields. The use of the three sets of samples allows the effects of grain size on the responses of the materials to be analyzed. During the experiments, the environment temperature and humidity are 296.3 ± 0.25 K and 42.9 ± 0.8 % , respectively.

Deformation Mechanisms

Under compression, the sucrose grains are fractured and smaller crushed particles hold together and form a coherent compact, in what is known as the briquetting process. Sucrose has a high level of briquetting tendency under compression, unlike other organic materials such as coal and sodium chloride [54]. Figure 9 shows an SEM image of material C $(\bar{d}_0 = 775\ \mu\text{m})$ after the experiment. This figure shows that some grains have sizes similar to the sizes of the initial grains, suggesting that these grains may not have fractured under

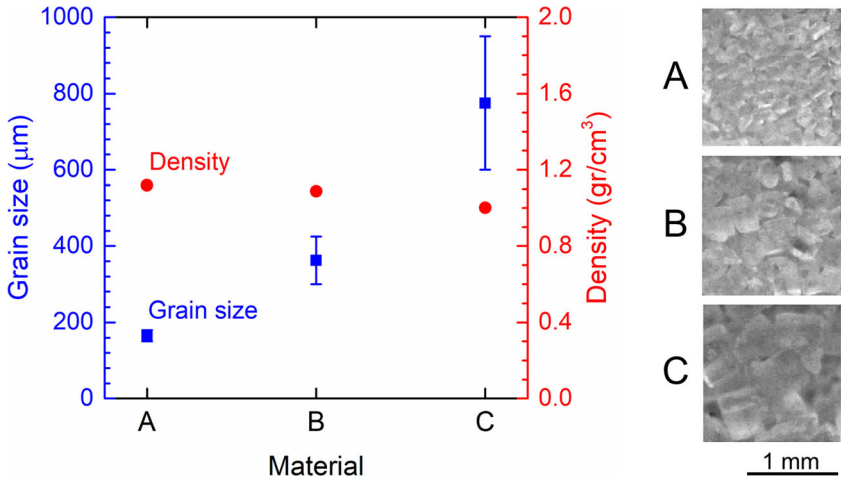

Fig. 7 Initial grain size and density of materials

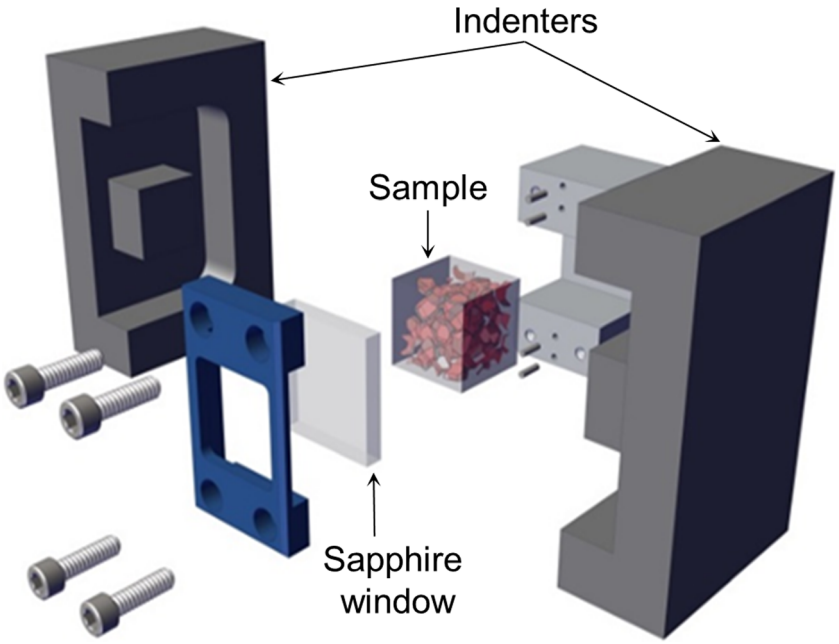

Fig. 8 Illustration of the confinement box, the sample, and the sapphire window for the compression experiments

loading. This figure also provides visual evidence of briquetting. Micro densification is important for achieving sufficient areas of contact between the particles in a compact in order for the whole sample to remain coherent after the pressure is released (i.e., briquetting). Although organic particles such as sodium chloride, coal, and sucrose are known to be brittle [55], these materials behave plastically if they are small and subjected to high levels of compressive stress [56]. The critical size of a particle for transition from fragmentation to plastic deformation is uncertain and varies over a considerable range of factors.

Figure 10 shows the stages of overall deformation (engineering strain, $\Delta L/L_0$, where $L_0 = 5$ mm is the initial length of the sample in the loading direction) in the materials as a function of time during the experiments. The overall strain in the sample is calculated using the relative positions of the indenters recorded in the VL images. Three stages are observed: (1) fragmentation of grains ($0 \le t < 0.56$ ms), (2) briquetting ($0.56 \le t < 1.18$ ms), and (3) unloading ($t \ge 1.18$ ms). The three materials show similar deformation trends; therefore, we mainly discuss material C in this section. Figure 10 also shows the times of the infrared images captured at a rate of one frame for every 20 visible images based on the framing rates of the two cameras. In addition, this figure denotes the infrared images with and without temperature increase.

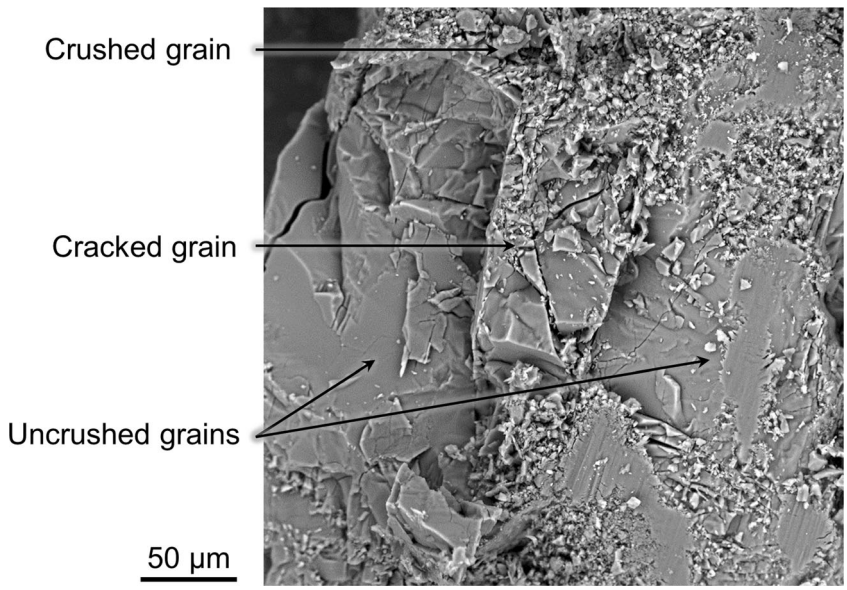

Fig. 9 SEM image of material C after the experiment

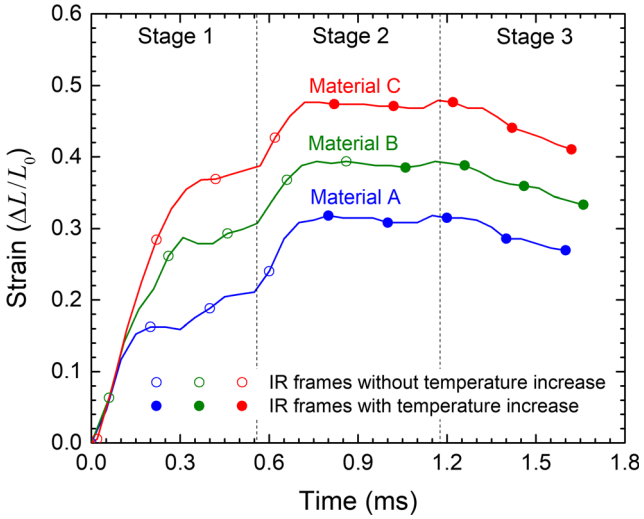

Fig. 10 Overall strain in the material as a function of time. The solid and hollow circles show the temperature frames with and without temperature increase, respectively

In the first stage of deformation ($0 \le t < 0.56$ ms), material C (sieve 30) is compressed by 38% and inter-granular void collapse occurs, as shown in Fig. 11. Fine grains ($d \le 50$ μm) resulting from fragmentation flow between large grains ($d \ge 250$ μm) and fill the voids in between. The filled voids do not experience as extensive deformation as unfilled voids. In this stage, the IR camera captures two infrared images and neither shows appreciable temperature increase. In the second stage of deformation ($0.56 \le t < 1.18$ ms), the material is further compressed by 10% and unlike in the first stage, a limited amount of fragmentation is observed. Four IR images are captured in this stage, with the latter two images showing increases in temperature inside the material. In the last stage ($t \ge 1.18$ ms), partial unloading occurs as the overall strain decreases from 47.1% to 41.2%. The two IR images associated with the third stage show significant temperature increase in the material.

Temperature Fields

The two major heating mechanisms in the materials are plastic deformation and friction. Sucrose is known to be brittle in general, but can deform plastically if the grains are small and high levels of compressive stresses are present. According to our observations, grain fragmentation in the first stage does not directly lead to heat generation; however, fragmentations affect heat generation by facilitating inelastic deformation and, more importantly, localized frictional heating along fragmented faces.

Experimentally, it is challenging to quantify the contribution of each underlying mechanism to the formation of hotspots. However, the simultaneous visible and infrared images allow the locations of the hotspots with respect to microstructure features to be identified. The localized temperature spikes or hotspots are responsible for thermal softening, thermal runaway, and ignition in energetic materials. Identification of the locations of the hotspots is important for understanding the underlying mechanisms leading to formation of the hotspots. For example, a hotspot inside a grain and far from interfacial boundaries most likely results from inelastic deformation, while a hotspot at a boundary likely results

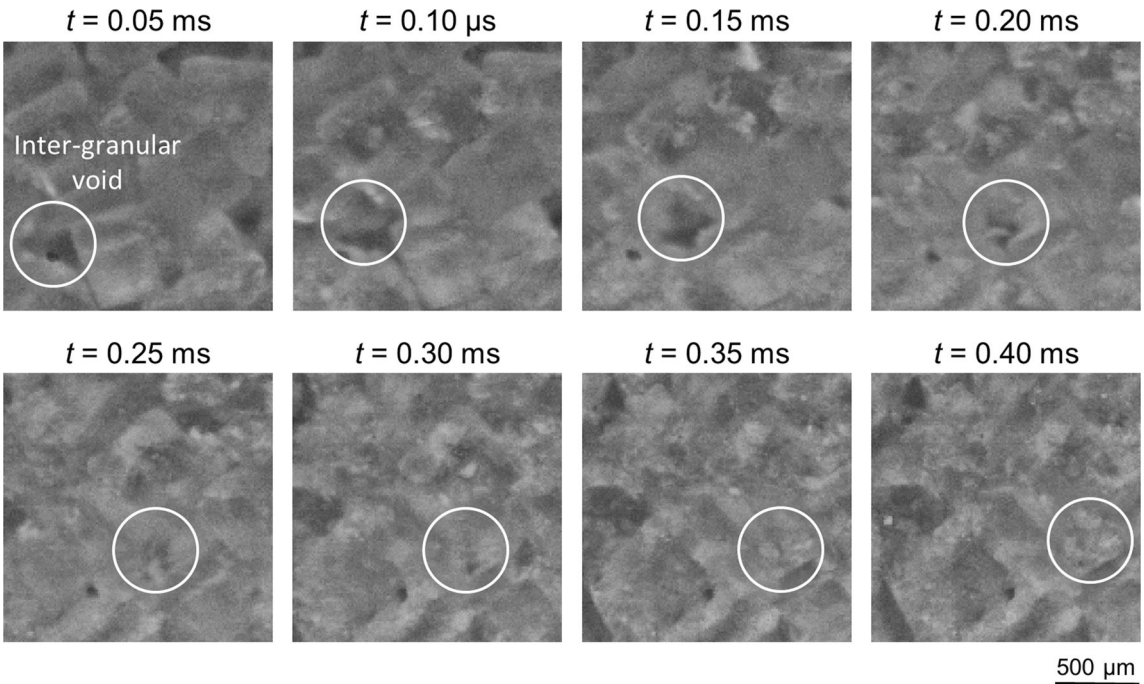

Fig. 11 Visible image sequence of inter-granular void collapse (material C)

from frictional dissipation. In addition, knowledge of the potential locations of hotspots can be used to modify the local thermo-mechanical response of materials by changing the constituent and interfacial properties.

Figure 12(a) and (b) show a sequence of visible images and the corresponding temperature fields for material C, respectively. The first infrared image showing temperature increase is captured at $t = 0.8$ ms, which occurs in the second stage of deformation. Due to the highly non-uniform stress distributions, some grains experience little deformation or failure. As a result, a few large grains ($d \geq 250$ μm) remain in the briquette. Inelastic deformation occurs after micro-squashing. Therefore, unfragmented or partially fragmented grains show little plastic deformation in the interior but mostly frictional heating and deformation at or near the boundaries. The boundaries of larger grains are the primary locations of hotspots, as shown in Fig. 12(b), suggesting the primary role of interfacial friction in the formation of these hotspots.

Variations in grain size of the materials provide perturbations to the thermo-mechanical processes, causing temperature distributions to differ. Figure 13 shows the temperature distributions in the three materials at $t = 1.23$ ms. Despite the higher overall temperature levels, the temperature fields in the materials with smaller grain sizes (materials A and B) are less localized. Materials with smaller grains experience more energy dissipation, since smaller grains are more likely to undergo plastic deformation, and their high surface to volume ratios facilitate frictional dissipation. As a result, the samples with smaller initial grain sizes show higher amounts of heating and higher overall temperatures than materials with larger grain sizes. However, despite the higher amounts of overall heat generation, the materials with smaller grains have lower levels of peak temperatures. This reduction in localized heating results from two factors. First, energy dissipation from plastic deformation spreads more widely in and is less localized. Second, frictional heating is more uniformly distributed since more sites for frictional heating exist.

Figure 14(a) and (b) show the average temperature and the peak temperature levels of the materials. The materials with larger grain sizes have lower average temperatures but higher peak temperatures. Specifically, the difference between the average and peak temperatures in material A $\left(\overline{d}_0 = 165\ \mu\text{m}\right)$ is only 1.3 K, while the difference in material C $\left(\overline{d}_0 = 775\ \mu\text{m}\right)$ is 16.5 K. The uncertainty in temperature measurements is 0.5 K according to calibration data. The correlation between local deformation and temperature in hotspots is discussed in the next section.

Digital Image Correlation (DIC) Analysis of Deformation

Hotspots result from various deformation mechanisms; therefore, the deformation fields are very useful in the determination of dominant mechanisms contributing to the formation of hotspots. To obtain the strain fields, we performed digital image correlation (DIC) analysis, a widely used non-contact technique for measuring material deformation. The analysis is carried out with the Ncorr, an open-source subset-based package with enhanced algorithms [57]. This package uses the reliability-guided digital image correlation (RG-DIC) framework [58]. Since displacements are at discrete locations, strain fields calculated directly from displacements tend to be

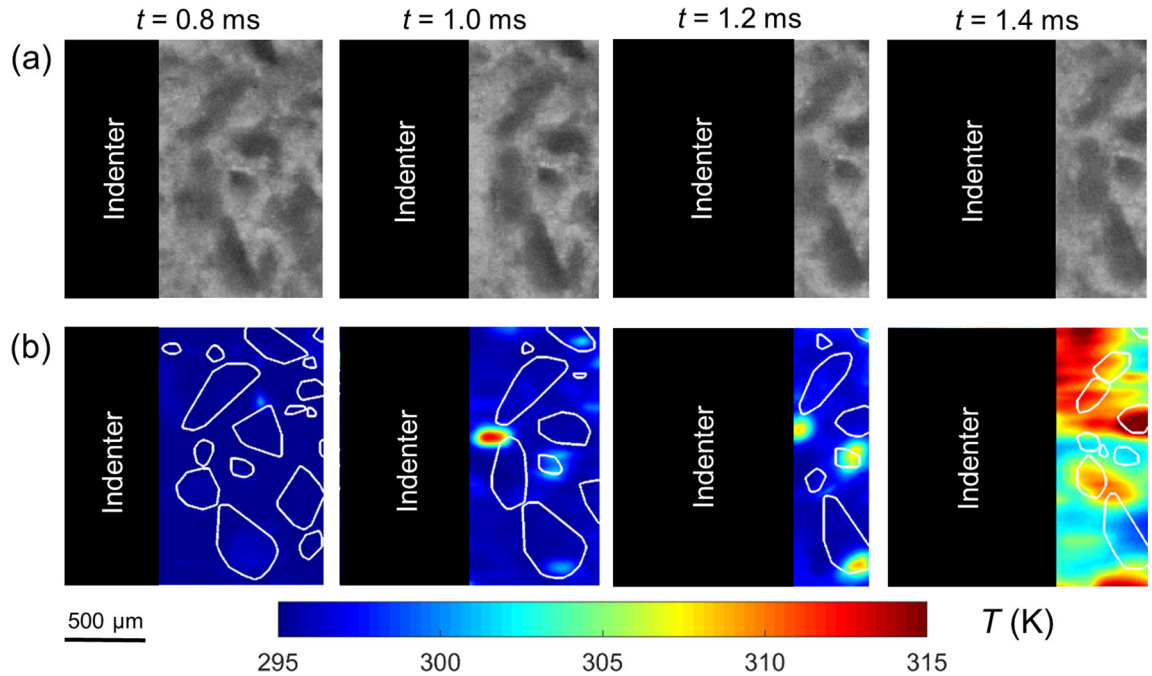

Fig. 12 Visible and infrared image sequences of material C. No temperature increase is observed for $t < 0.8$ ms

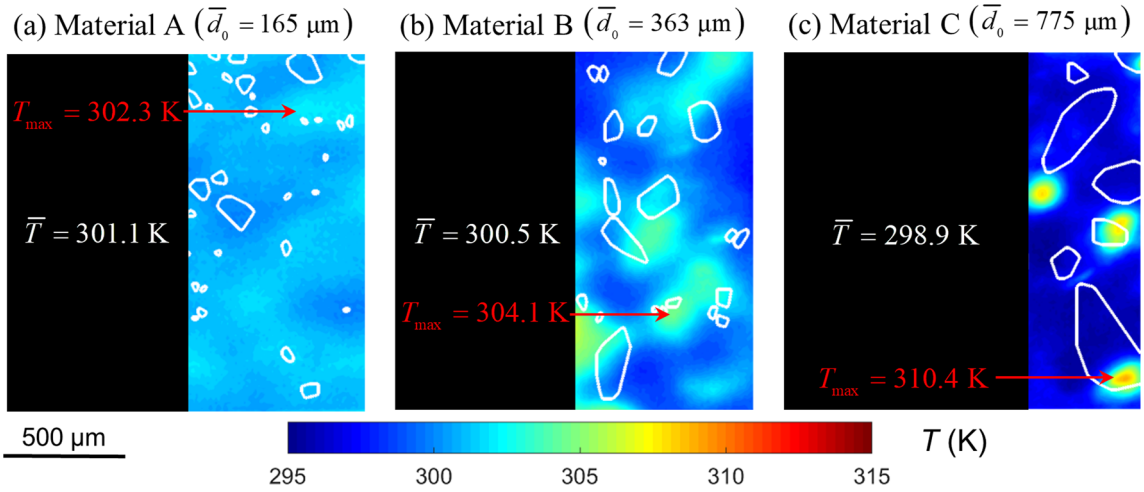

Fig. 13 Temperature fields in the materials at $t = 1.23$ ms; (**a**) material A, (**b**) material B, and (**c**) material C

noisy and unreliable. To address this issue, Ncorr uses a 2D Savitzky-Golay (SG) digital differentiator based on the principle of local least-square fitting with two-dimensional polynomials [59].

DIC analysis assumes displacement continuity in the region of interest (ROI) where the correlation is performed. The incorporation of discontinuities in DIC analyses is an open problem in the literature. For the cases when the discontinuity path is known, the displacement field on each side of the discontinuity can be analyzed separately [60]. A potential drawback of this approach is that the displacements at or near the discontinuities/interfaces cannot be calculated directly. We are aware of attempts to obtain the displacements in the neighborhood of an interface via extrapolation. Even so, traction continuity across the interface cannot be ensured. A DIC analysis is even more complex and less reliable when arbitrary crack initiation sites and propagation paths exist. Because of these reasons and the significant fragmentation in the first stage of deformation, the DIC analysis is only performed for the second stage of deformation when the material is briquetted. Therefore, the obtained strain fields from the DIC analysis are not representative of the total deformation from the very beginning of loading. In general, out-of-plane movements of grains are unavoidable and these movements partially degrade the DIC results. Out-of-plane movements of grains are restricted during the second stage as a result of briquetting. After briquetting, the sample has planar surfaces. These surfaces remain planar during the deformation process as a result of confinement. For confined compacted sugar samples, Forsberg and Siviour (2009) performed 2D-DIC and 3D digital volume correlation (DVC), and showed that the results of 2D and 3D analysis are very close [61]. To estimate the distortion levels of IR and VL images, we used distortion targets which consist of arrangement of identical speckles with known distances. The long-distance microscope lenses used for the IR and VL imaging showed negligible levels of distortion.

Figure 15 shows the reference image, the final image, and the subset size with respect to the microstructure for the DIC analysis. The natural pattern of the briquette is used for the DIC analysis [61]. To compensate for the lack of a speckle pattern, a large circular subset with a diameter of 50 pixels (0.67 mm) and a total number of 1964 pixels is used. The subset size is large enough to circumscribe the largest grain

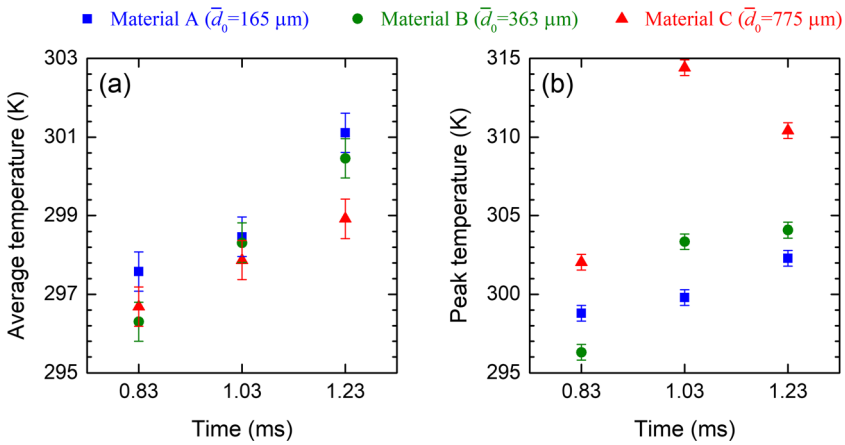

Fig. 14 (**a**) Average temperature levels in the materials and (**b**) peak temperature levels in the materials as functions of time. At $t = 0.83$ ms, material B $(\bar{d}_0 = 363\ \mu m)$ is at the initial temperature state. The error bars show the uncertainty in temperature measurements

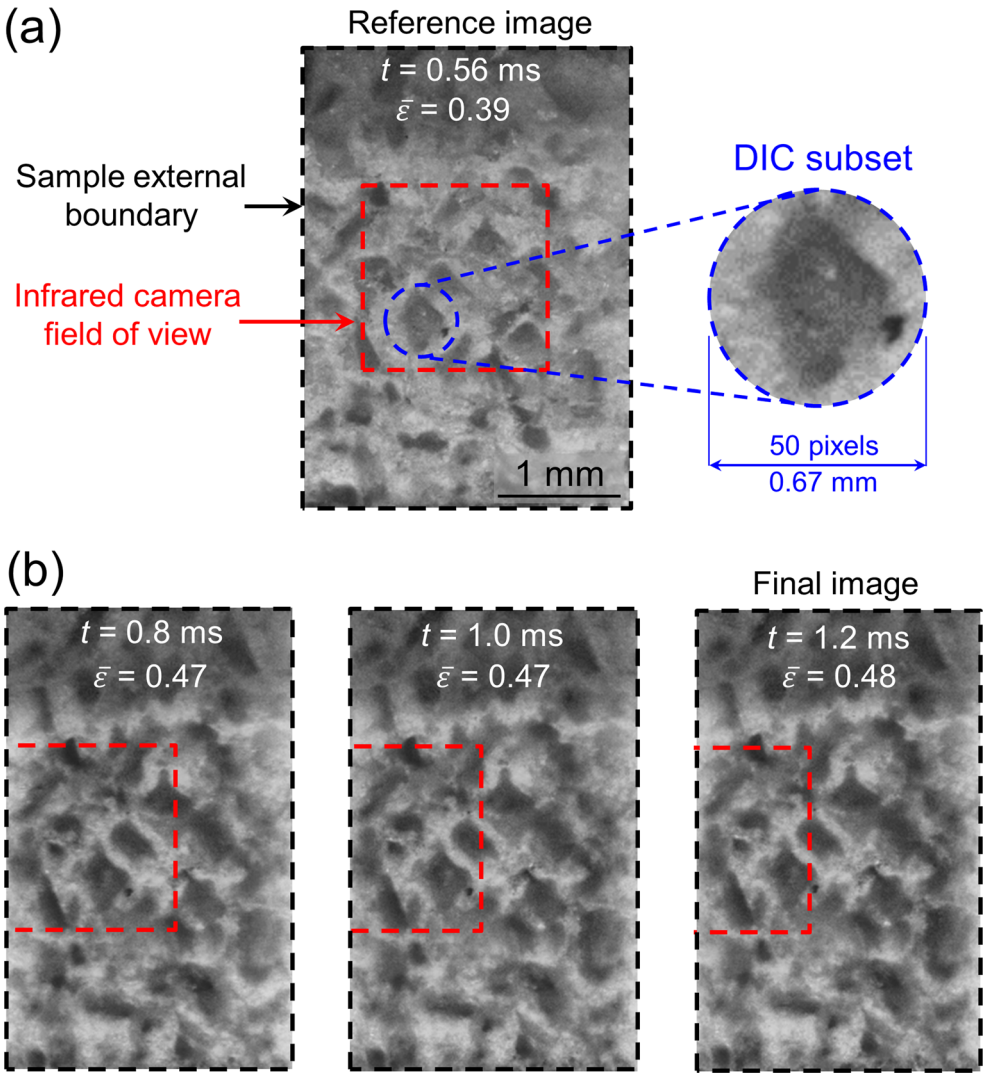

Fig. 15 (**a**) The reference image and the subset size, and (**b**) 2 out of the 63 intermediate frames and the final image used for the DIC analysis. The black dash line shows the external boundaries of the sample and the red dash line shows the FOV of the IR camera

in the reference image [see Fig. 15(a)]. In the second stage, the average stain rate is 153 s^{-1} and the maximum strain rate is 697 s^{-1} which occurs at the beginning of this stage. Therefore, with a temporal resolution of 10 μs, the average strain increase between successive frames is 1.5×10^{-3} and the maximum strain increase between successive frames is 7×10^{-3} which occurs only for the first few frames.

Figure 16 shows the temperature and Almansi strain fields of material C at $t = 1.0$ and 1.2 ms. The Almansi strain tensor is defined through

$$\varepsilon = \frac{1}{2}\left(\mathbf{I} - \mathbf{F}^{-T}\mathbf{F}^{-1}\right), \tag{3}$$

where $\mathbf{I}$ and $\mathbf{F}$ are the second-order identity and the deformation gradient tensors, respectively. The superscripts "-*T*" and "-1" denote the inverse transpose and inverse of tensors, respectively. The strain fields show the local deformation in the sample from the beginning of the second stage of deformation ($t = 0.56$ ms). Therefore, these strain fields are not representative of the total deformation in the sample since the very beginning of loading. Since the temperature of the material does not begin to increase appreciably until the latter part of the second stage of deformation, the deformation mechanisms involved in the second stage are primarily responsible for the temperature increase in the material. The strain fields indicate highly heterogeneous deformation. The normal strains show regions of instantaneous expansion and contraction in both axial directions. The shear strains show vertices or shear in both the clockwise and counterclockwise directions. These features are consistent with the flow of granular materials.

Correlation between Deformation and Temperature in Hotspots

With the VL and IR image sequences, the unique MINTED capability allows the determination and tracing of the trajectories of hotspots or material points with respect to the

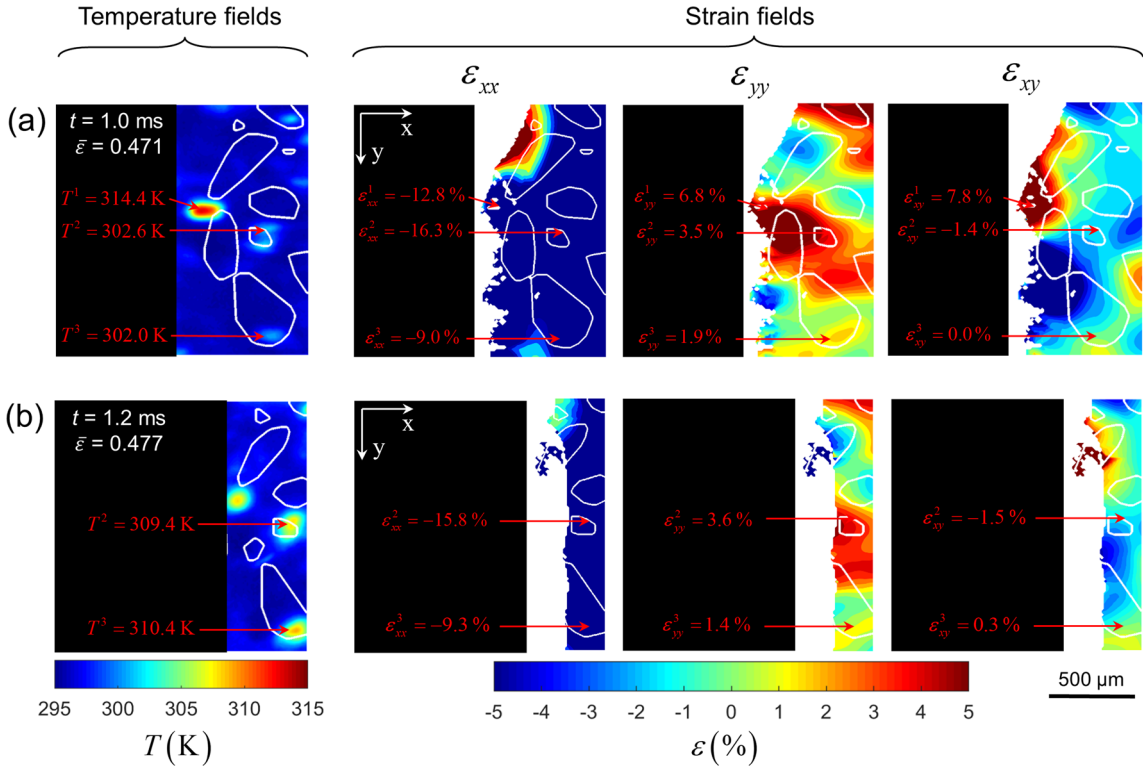

Fig. 16 Temperature and strain fields for material C; (**a**) $t = 1.0$ ms, and (**b**) $t = 1.2$ ms. These strain fields show the local deformation in the sample from the begining of the second stage of deformation ($t = 0.56$ ms)

microstructure. To achieve this, the VL and IR images are first spatially and temporally synchronized. The hotspot or material point $\mathbf{X}_i$ has position $\mathbf{x}_i = \mathbf{x}_i(\mathbf{X}_i, t)$ at time t. This position is obtained by solving the for $\mathbf{x}_i$ in the form of

$$\mathbf{x}_i = \mathbf{X}_i + \mathbf{u}(\mathbf{x}_i, t), \tag{4}$$

where $\mathbf{u}(\mathbf{x}_i, t)$ is the Eulerian displacement measured at $\mathbf{x}_i$ at t. Figure 16(a) shows three hotspots in the sample at $t = 1.0$ ms and the corresponding local strains. Two of these hotspots are traced and their temperatures and local strains are captured at $t = 1.2$ ms [Fig. 16(b)].

Although the overall strain essentially ceases to evolve in the second half of the second stage of deformation, a fraction of the input work stored in the sample dissipates over time, causing local deformation to continue and temperature to increase further. As evidence, Fig. 16 compares the temperature and strains of two hotspots (denoted with T^2 and T^3) at $t = 1.0$ and 1.2 ms, when the overall strain of the sample remains constant ($\bar{\varepsilon} \cong 0.47$). The temperature increases in the two hotspots from $t = 1.0$ ms to $t = 1.2$ ms are accompanied by increases in the local shear strain (ε_{xy}) in the hotspots. Specifically, the 8.4 K increase in the temperature of hotspot 3 (labeled with T^3 in Fig. 16) is associated with a ~0.3% increase in ε_{xy}.

Figure 17(a) quantifies the number and average area of hotspots whose interior temperatures are above or at temperature T in Fig. 16(b). Figure 17(b) quantifies the deformation modes (volumetric and maximum shear strains) for the hotspots in Fig. 16(b). The two major heating mechanisms in the materials are plastic deformation and friction, both of which result from shear deformation beyond certain limits. It is challenging to separate the contributions of the two mechanisms without additional information. In this regard, our recent computational simulations can provide more details [62]. Both volumetric strain and maximum shear strain levels are higher in the hotspots with higher temperatures and the shear deformation is more pronounced in the hotspots. The results show a direct correlation between maximum shear strain and temperature levels in hotspots.

Effect of Subset Size on Computation of Local Deformation Levels

Proper selection of subset size relative to the length-scale of physical features is important in DIC analyses. Smaller subsets yield better resolutions for small-scale features while larger subsets cause more averaging and may be appropriate for larger-scale features. Results obtained from smaller subsets contain higher levels of noise that may obscure small-scale physical features. Large subsets reduce noise levels but may not allow capture of small-scale physics. In addition, a subset needs to be large enough to track an arrangement of speckles/features in order to perform correlation. In the experiments

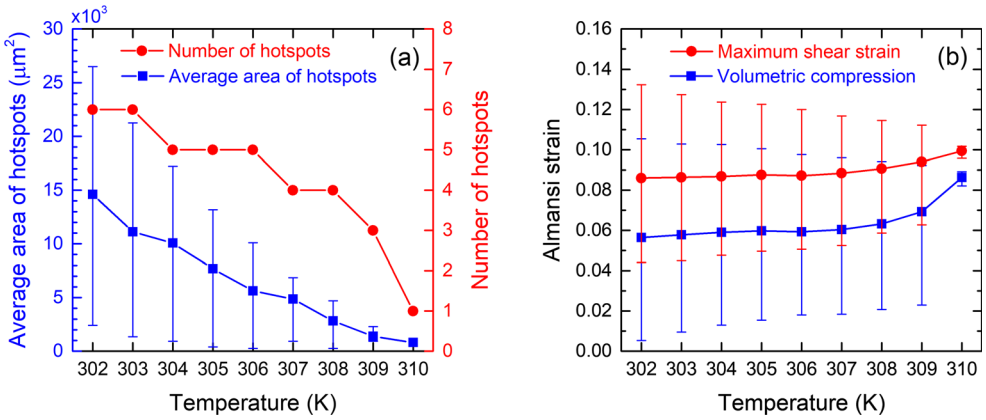

Fig. 17 (**a**) Number and average area of hotspots whose interior temperatures are above or at temperature T, and (**b**) local volumetric and maximum shear Almansi strains in hotspots as functions of hotspot temperature for material C at $t = 1.2$ ms [Fig. 16(b)]

here, the natural pattern of the briquetted sample is used for the DIC analysis. To compensate for the lack of a speckle pattern, the subset needs to be large enough to capture boundaries of grains in order to calculate the deformation fields inside grains. Therefore, a large circular subset with a diameter of 0.67 mm (50 pixels) that circumscribes the largest grain in the sample is used [see Fig. 15(a)].

Hotspots are important physical features in the experiments performed here. Hotspot 2 (labeled with T^2 in Fig. 16) is at the boundary of a small grain with a size of 0.173 mm next to another grain with a size of 0.3 mm. Therefore, a good correlation can be achieved even with subset sizes smaller than 0.67 mm (50 pixels) for the neighborhood of hotspot 2. Figure 18 shows the strain components associated with hotspot 2 at $t = 1.0$ and 1.2 ms for subset sizes $0.4 - 0.94$ mm ($30 - 70$ pixels). The smallest subset with a size of 0.4 mm (30 pixels) yields the highest level of ε_{xy} but the lowest levels of ε_{xx} and ε_{yy} in hotspot 2. As the subset size increases to 0.94 mm (70 pixels), ε_{xy} decreases and the normal strains (i.e., ε_{xx} and ε_{yy}) reach constant levels. The increase in ε_{xy} with decreasing the subset size shows that the shear deformation is more localized. Since this localized deformation occurred at a grain boundary, this shear deformation results from friction. This observation is consistent with what we see in our recent computational study [62]. In addition, the increase in ε_{xy} associated with the 6.4 K increase in the temperature of hotspot 2 from $t = 1.0$ ms to $t = 1.2$ ms is perspicuous with small subsets. Specifically, the increase in ε_{xy} from $t = 1.0$ ms to $t = 1.2$ ms is 1.4% for the subset size of 0.4 mm (30 pixels) while the increase is only 0.1% for the subset size of 0.64 mm (50 pixels).

Conclusion

A novel capability (**MINTED**, or **m**icroscale ***in-situ*** imaging of **te**mperature and **d**eformation fields under dynamic loading) for time-resolved and space-resolved measurements of the temperature and deformation fields at the microstructure level for dynamic conditions is developed. The method integrates a state-of-the-art high-speed infrared (IR) camera and a high-speed visible light (VL) camera in a split-Hopkinson pressure bar (SHPB) or Kolsky bar apparatus. To simultaneously capture deformation and temperature fields at normal incidence, the visible (VL) and infrared (IR) emissions from the sample are separated by a dichroic beam splitter. The beam splitter reflects VL light and directs the light into the VL camera. This is a general capability that can be used to study

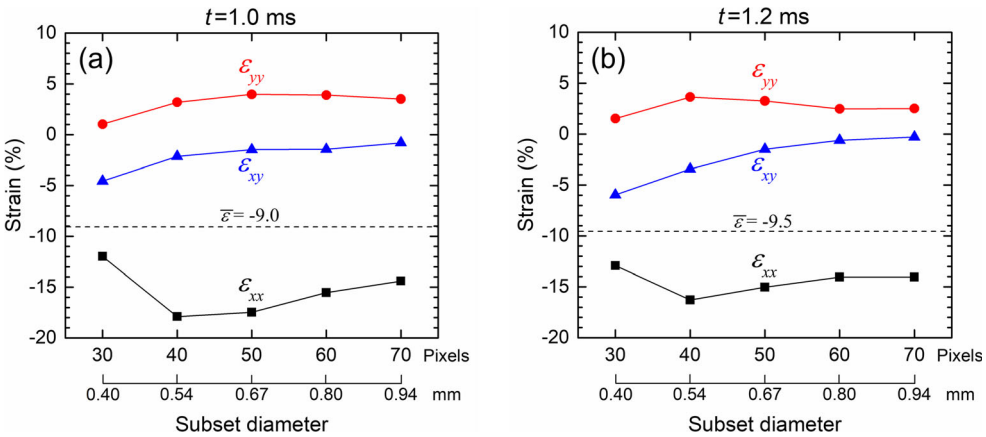

Fig. 18 Variations in local strains (ε_{xx}, ε_{yy}, and ε_{xy}) inside hotspot 2 (labeled with T^2 in Fig. 16) during the second stage of deformation as a function of subset size; (**a**) $t = 1.0$ ms, and (**b**) $t = 1.2$ ms. Here, $\bar{\varepsilon}$ denotes the overall strain occurred in the sample during the second stage of deformation

deformation, failure and heating in a range of materials, including metals, composites, ceramics, soft materials, and energetic materials.

To demonstrate the capabilities of the MINTED system, we performed experiments on sucrose granules, which are widely used as a simulant of energetic crystals. The experiments involve three sucrose materials with the average grain sizes of 165, 362.5, and 775 μm. The samples are confined in a box behind a sapphire window. Under loading, the grains are fragmented, squashed, and briquetted. The materials undergo significant temperature increases in the briquetting stage. Despite higher overall temperature levels, the temperature fields in the materials with smaller grain sizes are less localized. The unique capability here for simultaneous measurements of deformation and temperature fields allows the determination and tracing of the locations of hotspots or material points with respect to the material microstructure features. The results show that the boundaries of unfragmented grains are the primary locations of hotspots. The maximum shear strain levels are locally higher than volumetric strain levels in the hotspots, and there is a direct correlation between maximum shear strain and temperature levels in hotspots.

Acknowledgements The authors gratefully acknowledge support from the Air Force Office of Scientific Research through grant FA9550-15-1-0499 (Dr. Martin Schmidt). Experiments were performed at the Dynamic Property Research Laboratory (DPRL) at Georgia Tech.

References

1. Hartley KA, Duffy J, Hawley RH (1987) Measurement of the temperature profile during shear band formation in steels deforming at high strain rates. J Mech Phys Solids 35(3):283–301. https://doi.org/10.1016/0022-5096(87)90009-3
2. Marchand A, Duffy J (1988) An experimental study of the formation process of adiabatic shear bands in a structural steel. J Mech Phys Solids 36(3):251–283. https://doi.org/10.1016/0022-5096(88)90012-9
3. Zhou M, Rosakis AJ, Ravichandran G (1996) Dynamically propagating shear bands in impact-loaded prenotched plates—I. Experimental investigations of temperature signatures and propagation speed. J Mech Phys Solids 44(6):981–1006. https://doi.org/10.1016/0022-5096(96)00003-8
4. Guduru PR, Rosakis AJ, Ravichandran G (2001) Dynamic shear bands: an investigation using high speed optical and infrared diagnostics. Mech Mater 33(7):371–402. https://doi.org/10.1016/S0167-6636(01)00051-5
5. Li Z, Lambros J (2001) Strain rate effects on the thermomechanical behavior of polymers. Int J Solids Struct 38(20):3549–3562. https://doi.org/10.1016/S0020-7683(00)00223-7
6. Li Z, Lambros J (2000) Dynamic thermomechanical behavior of fiber reinforced composites. Compos A: Appl Sci Manuf 31(6):537–547. https://doi.org/10.1016/S1359-835X(99)00102-5
7. Goretta KC, Park ET, Koritala RE, Cuber MM, Pascual EA, Chen N, de Arellano-López AR, Routbort JL (1998) Thermomechanical response of polycrystalline $BaZrO_3$. Physica C 309(3):245–250. https://doi.org/10.1016/S0921-4534(98)00588-7
8. Mukherjee K, Sircar S, Dahotre NB (1985) Thermal effects associated with stress-induced martensitic transformation in a Ti-Ni alloy. Mater Sci Eng 74(1):75–84. https://doi.org/10.1016/0025-5416(85)90111-9
9. McCormick PG, Liu Y, Miyazaki S (1993) Intrinsic thermal-mechanical behaviour associated with the stress-induced martensitic transformation in NiTi. Mater Sci Eng A 167(1):51–56. https://doi.org/10.1016/0921-5093(93)90336-D
10. Field J, Bourne N, Palmer S, Walley S, Sharma J, Beard B (1992) Hot-spot ignition mechanisms for explosives and propellants [and discussion]. Philos Trans R Soc London A 339(1654):269–283. https://doi.org/10.1098/rsta.1992.0034
11. Field JE, Swallowe GM, Heavens SN (1982) Ignition mechanisms of explosives during mechanical deformation. Proc R Soc London A 382(1782):231–244. https://doi.org/10.1098/rspa.1982.0099
12. Tarver CM, Chidester SK, Nichols AL (1996) Critical conditions for impact- and shock-induced hot spots in solid explosives. J Phys Chem 100(14):5794–5799. https://doi.org/10.1021/jp953123s
13. Winter RE, Field JE (1975) The role of localized plastic flow in the impact initiation of explosives. Proc R Soc London A 343(1634):399–413. https://doi.org/10.1098/rspa.1975.0074
14. Guirguis RH (2000) Ignition due to macroscopic shear. AIP Conf Proc 505(1):647–650. https://doi.org/10.1063/1.1303556
15. Skidmore C, Phillips D, Asay B, Idar D, Howe P, Bolme D (2000) Microstructural effects in PBX 9501 damaged by shear impact. AIP Conf Proc 505(1):659–662. https://doi.org/10.1063/1.1303559
16. Menikoff R (2005) Elastic-plastic response of HMX. Research highlights.
17. Ravindran S, Tessema A, Kidane A (2017) Multiscale damage evolution in polymer bonded sugar under dynamic loading. Mech Mater 114:97–106. https://doi.org/10.1016/j.mechmat.2017.07.016
18. Bloomquist D, Sheffield S (1981) Shock-compression temperature rise in polymethyl methacrylate determined from resistivity of embedded copper foils. Appl Phys Lett 38(3):185–187. https://doi.org/10.1063/1.92272
19. Bloomquist D, Sheffield S (1980) Thermocouple temperature measurements in shock-compressed solids. J Appl Phys 51(10):5260–5266. https://doi.org/10.1063/1.327480
20. Boboridis K, Obst AW (2003) A high-speed four-channel infrared pyrometer. AIP Conf Proc 684(1):759–764. https://doi.org/10.1063/1.1627219
21. Long DA (1977) Raman spectroscopy. McGraw-Hill, New York
22. Yuan V, Bowman JD, Funk D, Morgan G, Rabie R, Ragan C, Quintana J, Stacy H (2005) Shock temperature measurement using neutron resonance spectroscopy. Phys Rev Lett 94(12):125504. https://doi.org/10.1103/PhysRevLett.94.125504
23. Dolan DH, Ao T, Seagle CT (2013) Reflectance thermometry in dynamic compression experiments. AIP Conf Proc 1552(1):767–770. https://doi.org/10.1063/1.4819639
24. Dolan DH, Seagle CT, Ao T (2013) Dynamic temperature measurements with embedded optical sensors. SANDIA report no SAND2013-8203.
25. Coffey C, Jacobs S (1981) Detection of local heating in impact or shock experiments with thermally sensitive films. J Appl Phys 52(11):6991–6993. https://doi.org/10.1063/1.328664
26. Zehnder AT, Rosakis AJ (1991) On the temperature distribution at the vicinity of dynamically propagating cracks in 4340 steel. J Mech Phys Solids 39(3):385-415. https://doi.org/10.1016/0022-5096(91)90019-K
27. Costin L, Crisman E, Hawley RH, Duffy J (1980) On the localisation of plastic flow in mild steel tubes under dynamic torsional loading. Proc 2nd Conf mechanical properties of materials at high rates of strain, Oxford, England, pp 90–100.
28. Soudre-Bau L, Meshaka Y, Parent G, Boulet P, Le Corre B, Jeandel G (2013) Combined temperature and deformation measurement during glass forming in a real scale setup. Exp Mech 53(9):1773–1781. https://doi.org/10.1007/s11340-013-9764-z

29. Bodelot L, Charkaluk E, Sabatier L, Dufrénoy P (2011) Experimental study of heterogeneities in strain and temperature fields at the microstructural level of polycrystalline metals through fully-coupled full-field measurements by digital image correlation and infrared thermography. Mech Mater 43(11):654–670. https://doi.org/10.1016/j.mechmat.2011.08.006
30. Bodelot L, Sabatier L, Charkaluk E, Dufrénoy P (2009) Experimental setup for fully coupled kinematic and thermal measurements at the microstructure scale of an AISI 316L steel. Mater Sci Eng A 501(1):52–60. https://doi.org/10.1016/j.msea.2008.09.053
31. Bertram Hopkinson FRS (1914) A method of measuring the pressure produced in the detonation of high, explosives or by the impact of bullets. Philos Trans R Soc London A 213(497-508):437–456. https://doi.org/10.1098/rsta.1914.0010
32. Kolsky H (1949) An investigation of the mechanical properties of materials at very high rates of loading. Proc Phys Soc B 62(11):676
33. Davies EDH, Hunter SC (1963) The dynamic compression testing of solids by the method of the split Hopkinson pressure bar. J Mech Phys Solids 11(3):155–179. https://doi.org/10.1016/0022-5096(63)90050-4
34. Staab GH, Gilat A (1991) A direct-tension split Hopkinson bar for high strain-rate testing. Exp Mech 31(3):232–235. https://doi.org/10.1007/bf02326065
35. Gilat A, Cheng C-S (2000) Torsional split Hopkinson bar tests at strain rates above $10^4 s^{-1}$. Exp Mech 40(1):54–59. https://doi.org/10.1007/bf02327548
36. Hartley K, Duffy J, Hawley R (1985) The torsional Kolsky (split-Hopkinson) bar. Metals handbook 8:218–228.
37. Wang QZ, Li W, Xie HP (2009) Dynamic split tensile test of flattened Brazilian disc of rock with SHPB setup. Mech Mater 41(3):252–260. https://doi.org/10.1016/j.mechmat.2008.10.004
38. Grantham SG, Siviour CR, Proud WG, Field JE (2004) High-strain rate Brazilian testing of an explosive simulant using speckle metrology. Meas Sci Technol 15(9):1867. https://doi.org/10.1088/0957-0233/15/9/025
39. Jiang F, Vecchio KS (2009) Hopkinson bar loaded fracture experimental technique: a critical review of dynamic fracture toughness tests. Appl Mech Rev 62(6):060802-060839. https://doi.org/10.1115/1.3124647
40. Chen R, Xia K, Dai F, Lu F, Luo SN (2009) Determination of dynamic fracture parameters using a semi-circular bend technique in split Hopkinson pressure bar testing. Eng Fract Mech 76(9):1268–1276. https://doi.org/10.1016/j.engfracmech.2009.02.001
41. Wang QZ, Feng F, Ni M, Gou XP (2011) Measurement of mode I and mode II rock dynamic fracture toughness with cracked straight through flattened Brazilian disc impacted by split Hopkinson pressure bar. Eng Fract Mech 78(12):2455–2469. https://doi.org/10.1016/j.engfracmech.2011.06.004
42. Zhao H, Gary G (1997) A new method for the separation of waves. Application to the SHPB technique for an unlimited duration of measurement. J Mech Phys Solids 45(7):1185–1202. https://doi.org/10.1016/S0022-5096(96)00117-2
43. Bacon C (1998) An experimental method for considering dispersion and attenuation in a viscoelastic Hopkinson bar. Exp Mech 38(4):242–249. https://doi.org/10.1007/bf02410385
44. Bacon C (1999) Separation of waves propagating in an elastic or viscoelastic Hopkinson pressure bar with three-dimensional effects. Int J Impact Eng 22(1):55–69. https://doi.org/10.1016/S0734-743X(98)00048-7
45. Frew D, Forrestal MJ, Chen W (2001) A split Hopkinson pressure bar technique to determine compressive stress-strain data for rock materials. Exp Mech 41(1):40–46. https://doi.org/10.1007/BF02323102
46. Song B, Chen W (2004) Dynamic stress equilibration in split Hopkinson pressure bar tests on soft materials. Exp Mech 44(3):300–312. https://doi.org/10.1007/bf02427897
47. Othman R (2018) The Kolsky-Hopkinson bar machine: selected topics. Springer International Publishing, Cham.
48. Lindholm US (1964) Some experiments with the split hopkinson pressure bar. J Mech Phys Solids 12(5):317–335. https://doi.org/10.1016/0022-5096(64)90028-6
49. Noble JP, Goldthorpe BD, Church P, Harding J (1999) The use of the Hopkinson bar to validate constitutive relations at high rates of strain. J Mech Phys Solids 47(5):1187–1206. https://doi.org/10.1016/S0022-5096(97)00090-2
50. Chen JJ, Guo BQ, Liu HB, Liu H, Chen PW (2014) Dynamic Brazilian test of brittle materials using the Split Hopkinson pressure bar and digital image correlation. Strain 50(6):563–570. https://doi.org/10.1111/str.12118
51. Hudspeth M, Claus B, Dubelman S, Black J, Mondal A, Parab N, Funnell C, Hai F, Qi ML, Fezzaa K, Luo SN, Chen W (2013) High speed synchrotron x-ray phase contrast imaging of dynamic material response to split Hopkinson bar loading. Rev Sci Instrum 84(2):025102. https://doi.org/10.1063/1.4789780
52. Yeager JD, Higginbotham Duque AL, Shorty M, Bowden PR, Stull JA (2018) Development of inert density mock materials for HMX. J Energ Mater 36(3):253–265. https://doi.org/10.1080/07370652.2017.1375049
53. Ramos K, Bahr D (2007) Mechanical behavior assessment of sucrose using nanoindentation. J Mater Res 22(7):2037–2045. https://doi.org/10.1557/jmr.2007.0249
54. Hardman J, Lilley B (1970) Deformation of particles during briquetting. Nature 228(5269):353. https://doi.org/10.1038/228353b0
55. Huffine CL (1953) A study of the bonding and cohesion achieved in the compression of particulate materials. Columbia University, New York City.
56. Bridgman PW (1952) Physics of high pressure. Bell, London.
57. Blaber J, Adair B, Antoniou A (2015) Ncorr: open-source 2D digital image correlation Matlab software. Exp Mech 55(6):1105–1122. https://doi.org/10.1007/s11340-015-0009-1
58. Pan B (2009) Reliability-guided digital image correlation for image deformation measurement. Appl Opt 48(8):1535–1542. https://doi.org/10.1364/AO.48.001535
59. Pan B, Xie H, Guo Z, Hua T (2007) Full-field strain measurement using a two-dimensional Savitzky-Golay digital differentiator in digital image correlation. Opt Eng 46(3):033601. https://doi.org/10.1117/1.2714926
60. Rubino V, Rosakis AJ, Lapusta N (2017) Understanding dynamic friction through spontaneously evolving laboratory earthquakes. Nat Commun 8:15991. https://doi.org/10.1038/ncomms15991
61. Forsberg F, Siviour CR (2009) 3D deformation and strain analysis in compacted sugar using x-ray microtomography and digital volume correlation. Meas Sci Technol 20(9):095703. https://doi.org/10.1088/0957-0233/20/9/095703
62. Keyhani A, Kim S, Horie Y, Zhou M (2018) Energy dissipation in polymer-bonded explosives with various levels of constituent plasticity and internal friction. Comput Mater Sci 159:136–149. https://doi.org/10.1016/j.commatsci.2018.12.008